International Journal of Plasticity 199 (2026) 104636

Contents lists available at ScienceDirect

International Journal of Plasticity

journal homepage: www.elsevier.com/locate/ijplas

Hetero-deformation mechanisms and GND-associated plastic strain partitioning across single/polycrystal hetero-boundary in nickel-based superalloys

Xinrui Xiao [a,b], Liwu Liu [a,*], Xiaoxian Zhang [a,*], Yanju Liu [a,b], Jinsong Leng [a]

[a] School of Astronautics, Harbin Institute of Technology, Harbin, 150001, China
[b] Suzhou Research Institute, Harbin Institute of Technology, Suzhou, 215100, China

ARTICLE INFO

Keywords:
Plastic deformation
Microstructure
Micromechanics modeling
Nickel-based superalloys
Heterogeneous Materials

ABSTRACT

The hetero-deformation mechanisms were systematically investigated using in-situ SEM and EBSD, combined with crystal plasticity finite element (CPFE) modeling. The results reveal that the softer single-crystal domain yields first due to the lower slip strength, accompanying by the lattice rotation and geometrically necessary dislocation (GND) accumulation near the single/polycrystal hetero-boundary (HB), which induces pronounced local hardening, thereby driving the sites of plastic strain accumulation shifting from HB to the interior of the single-crystal domain during the following cyclic loading. This GND density field is primarily controlled by the ΔE_{xx} (the difference of the elastic modulus along the loading direction), the minimum crystallographic misorientation (θ') between the <001> of the polycrystalline grain and the loading direction (nearly parallel to [010] of single-crystal grain), and the intrinsic slip strength on the both sides of HB. Low <001> misorientation ($\theta' \leq 15°$) or small ΔE_{xx} ($\leq$ 30 GPa), in combination with high geometric compatibility factor ($m' \geq 0.8$) decrease the demand for GND-associated compatibility near the HB. These results provide mechanistic insights for designing interfaces that enhance fatigue resistance and damage tolerance in the single/polycrystal nickel-based superalloys.

1. Introduction

Turbine disks and blades are critical components in aero engines and gas turbines (Peng et al., 2022). Nickel-based single-crystal superalloys, such as DD5, are commonly used for turbine blades due to their superior creep and fatigue resistance at high temperature (Li et al., 2021, Ren et al., 2022, Sato et al., 2011). These blades are typically coupled with polycrystalline superalloy disks (e.g., FGH96), which offer high strength and toughness. Compared to traditional blade-disk connection methods, such as mortise-and-tenon joints (Zou et al., 2024), integrally bladed disks (blisks) reduce weight by 20–30% and enhance both reliability and service life (Šajbanová et al., 2021, González-Barrio et al., 2020). Additionally, the integral design improves aerodynamic efficiency by minimizing heat transfer resistance and interfacial thermal barriers (Aschenbruck et al., 2014). However, the diffusion bonding of single-crystal blades to polycrystalline disks creates a hetero-boundary (HB) marked by mechanical and crystallographic discontinuities. This interface usually becomes a preferential site for strain localization and fatigue crack initiation (Liu and Nambu, 2024), posing challenges to structural integrity during service.

* Corresponding authors.
E-mail addresses: liuliwu_006@163.com (L. Liu), xiaoxian@hit.edu.cn (X. Zhang).

https://doi.org/10.1016/j.ijplas.2026.104636
Received 6 January 2026; Received in revised form 30 January 2026;
Available online 4 February 2026

Extensive efforts have been made to improve blisk fabrication processes, including diffusion bonding (Shi et al., 2023, Wu et al., 2023), additive manufacturing (Wang et al., 2024), and transient liquid-phase bonding (Li et al., 2022). However, the fundamental of deformation mechanisms near the single/polycrystal HBs remains elusive. These HBs are heterostructures with significant mechanical incompatibility between the domains (Zhu and Wu, 2023), which results in strain partitioning and accumulation of GNDs at the HB (Griesbach et al., 2024, Ma et al., 2023, Liu et al., 2025, Li et al., 2025). Such hetero-deformation phenomena are commonly observed at crystalline–amorphous boundaries (Fu et al., 2025), ceramic-metal phases (Peterson et al., 2024), phase boundaries in alloys (Nie et al., 2025) and the interface between coarse-grained and ultrafine-grained regions of the same material (Sun et al., 2022, Wang et al., 2020, Liu et al., 2020). These studies show that the carefully designed hetero-zones can leverage this effect to enhance strength and ductility through hetero-deformation induced (HDI) hardening (Xu et al., 2024, Najmabad et al., 2024, Zhang et al., 2024, Ran et al., 2024). In grain-scale, the micromechanical behaviors near these HBs are strongly associated with the crystallography and elastic modulus. The grain orientation of the nickel-based polycrystalline substrate determines the growth direction of the columnar grains (Wang et al., 2024), while deviations in single-crystal alloys affect mechanical behavior (Li et al., 2021, Qu et al., 2024, Wang et al., 2023). Crystal orientation also determines the elastic modulus along the loading direction (Zou et al., 2024), introducing the elastic mismatch that governs local deformation and damage (Zhang et al., 2021). The aforementioned factors result in a complex stress state that activates slip systems near the HBs, affecting the Luster–Morris factor m' (Li et al., 2025, Zhou et al., 2019, Chen et al., 2025), which is typically used to assess strain compatibility between adjacent grains (Chen et al., 2025, Escobar-Moreno et al., 2025, Chen et al., 2023). However, how these factors interact to control the GND distribution near the HB within the single-crystal domain, particularly the effect of the mismatch between the single-crystal loading direction and the polycrystal grain orientations, is yet to be systematically investigated and fully understood.

Despite considerable experimental efforts (Zhou et al., 2025, Zan et al., 2025), the spatial and temporal limitations of in-situ characterization hinder the quantification of local strain partitioning and GND density evolution. As a result, crystal plasticity finite element (CPFE) has been increasingly utilized to elucidate the underlying micromechanics in heterogeneous materials. The CPFE models have successfully captured size-dependent strengthening in heterostructures (Zhao et al., 2025, Zhang et al., 2024), the role of GNDs in gradient-grained materials (Zhang et al., 2023) and clarify how the strength disparities govern the strain partitioning by CPFE (Li et al., 2024). Recent work by Liu and Nambu (Liu and Nambu, 2024) employed CPFE to decouple the effects of interfacial hardening and DRX microstructure in Fe/Ni interface, demonstrating the critical importance of isolating competing factors. These models effectively describe mesoscale strain gradients on different materials and grain size gradient interfaces in polycrystalline metals. However, the modeling of heterogeneous interfaces between single crystal and polycrystalline materials within the same matrix (nickel-based alloys) represents a unique and unexplored scenario.

This study aims to clarify the deformation mechanisms near the single/polycrystal HB formed by diffusion bonding between single-crystal nickel-based superalloy DD5 and polycrystal nickel-based superalloy FGH96. We focus on the evolution of microstructure, plastic strain partitioning across the HB, and GND accumulation near the HB within the single-crystal domain. By integrating in-situ SEM/EBSD observations with the CPFE results, we decouple the effects of elastic mismatch along the loading direction (LD) and the minimum crystallographic misorientation between the loading direction (nearly parallel to the [010] of the single-crystal domain) and the <001> direction of the polycrystalline grains (θ'), associated with the geometric compatibility factor m'. Our findings reveal that low θ' combined with high m' results in minimal GND demand, indicating good interfacial compatibility, whereas high θ' with low m' promotes GND accumulation and plastic strain localization.

2. Methodology

2.1. Materials and experiment methods

In this study, polycrystal nickel-based superalloy FGH96 and single-crystal nickel-based superalloy DD5 were fabricated using the powder metallurgy process and directional solidification method, respectively. The nominal composition of the DD5 and the FGH96 are listed in Table 1. Before bonding, the faying surfaces were ground using SiC papers (400 to 2000 grit), followed by polishing with SiO_2 to achieve a surface roughness (Ra) of less than 0.85 μm (Liu and Nambu, 2024). Additionally, the materials were held at 1130°C under a compressive pressure of 12 MPa in a vacuum for 60 minutes, with heating and cooling rates of 4°C/s and 5°C/s, as shown in Fig. 1(a). The dimensions of the diffusion bonding sample are shown in Fig. 1(b), accompanied by a heated sleeve to modify the stress state near the joint interface, thereby reducing interfacial porosity and suppressing thermal crack initiation. Both superalloys are composed of a Ni-based solid solution (γ phase) and Ni_3Al precipitates (γ'), and their microstructures are shown in Fig. 1(c, d). Both DD5 and FGH96 possess a face-centered cubic (FCC) crystal structure, and the primary active slip system for plastic deformation is the {111}<110> system, which has been explicitly stated in the Appendix A. The inverse pole figure (IPF) and pole figure maps for FGH96 and DD5 are shown in Fig. 1(e-g). The polycrystal sample exhibits a nearly random crystal orientation, while the single-crystal domain displays a pronounced <001> texture, aligned with the loading direction (LD), corresponding to the directional solidification of DD5.

Table 1
Nominal composition (wt%) of the DD5 and FGH96.

Alloy	Cr	Co	Mo	W	Ta	Re	Al	Ti	Ni
DD5	7	8	2	5	6.5	3	6.2	–	Bal.
FGH96	16	13	4	4	–	–	2.2	3.7	Bal.

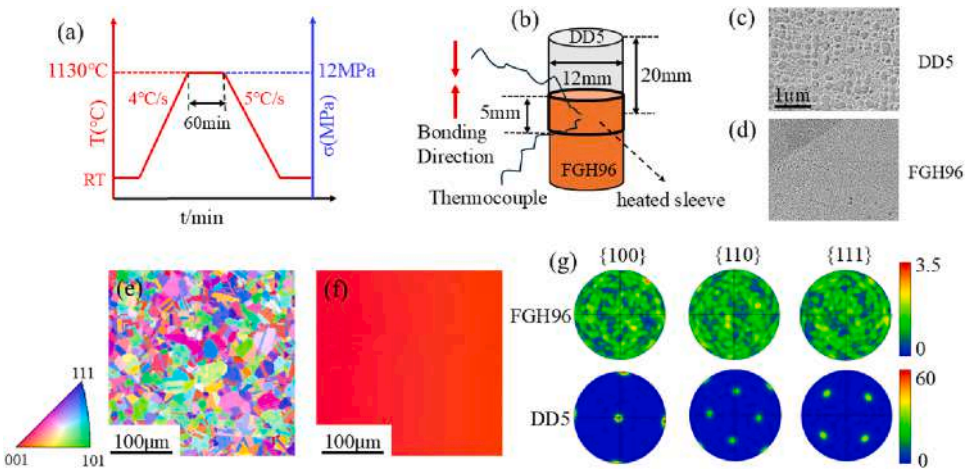

Fig. 1. Sample preparation and DB test: (a) temperature history of DB (b)dimensions of DB sample, (c) SEM microstructure of DD5 (d) SEM microstructure of FGH96 (e, f) IPF-X of FGH96 and DD5 (g) corresponding pole figure.

During test bar production, the specimen axis was aligned with the nominal [010] crystallographic orientation with a small deviation angle, This deviation angle is an inherent characteristic of the casting process and is difficult to eliminate completely, thus, a deviation of up to 10° is generally considered acceptable for practical applications (Raza et al., 2019). The deviation angle between the specimen axis and the <001> orientation of the single-crystal is approximately 3.5° in this study.

The free surface of the DB sample was initially ground with SiC papers of increasing fineness and then polished with a SiC suspension for 2 hours to remove the deformation layers. This preparation ensured a high-quality surface suitable for EBSD characterization. Electron backscatter diffraction (EBSD) measurements were performed at a 70° tilt, using a step size of 1 μm, square grid collection, an accelerating voltage of 20 kV before deformation on the region of interest (ROI). Dog-bone-shaped tensile specimens were machined from the center of the DB samples using electrical discharge machining (EDM), as shown in Fig. 2(a), with the ROI highlighted. The gauge section measured ~22 mm in length, 2 mm in width, and 1 mm in thickness, with the tensile loading axis aligned parallel to the specimen axis (global X-direction in Fig. 2(a)). Microstructural-sensitive finite element model was faithfully reconstructed based on the crystallographic orientation and morphological information obtained from the EBSD scan as shown in Fig. 2(b, c). Local deformation was monitored using a built-in extensometer mounted on the gauge section. The constant loading rate of 1 mm/min with an 810 MPa peak stress is cyclically conducted in TESCAN in-situ testing system, and the loading boundary condition of finite element model is same as the experiment, as shown in Fig. 2(d, e).

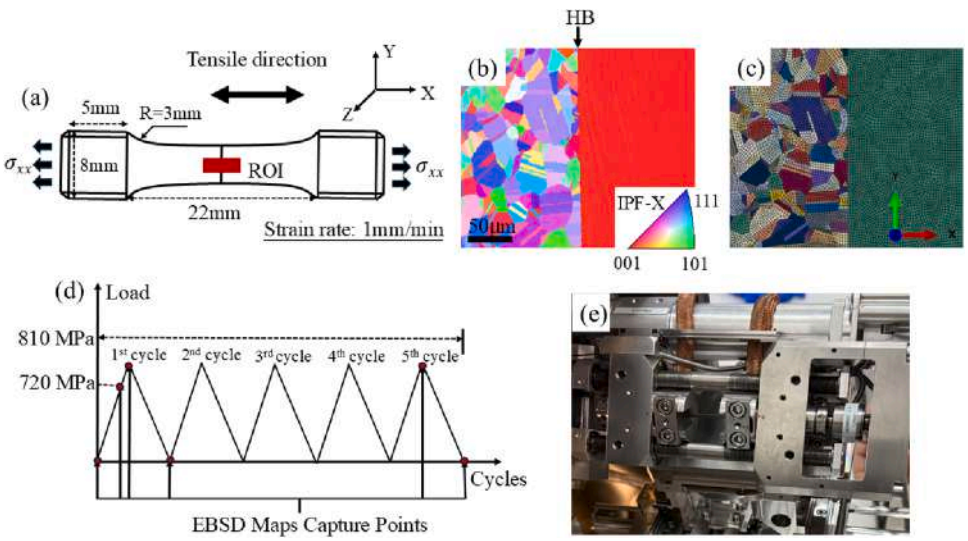

Fig. 2. (a) The dimensional drawing of the machined shape of the bonding sample and region of interest (ROI). (b) EBSD map of ROI (c) Finite element sub-model reconstructed from EBSD scans of ROI (d) Schematic diagram of loading profile in the in-situ tensile test (e) micro tensile stage system.

2.2. Computational methodology

Twenty-node 3D elements with reduced integration (C3D20R) were employed. In this study, the experimentally characterized 2D grain morphology on the observed surface from EBSD (shown in Fig. 2(b)) was extruded along the out-of-plane (Z) direction to construct a 3D geometry with a small thickness (3 μm ≤ 1/8 of the average grain size). This thickness was justified because the number of elements through the thickness has a negligible effects on the stress and strain response at the observed surface (Hardie et al., 2022, Wang et al., 2023). This "quasi-3D" approach is physically reasonable because the critical stress components governing plastic deformation are primarily in-plane on the observed free surface, while the out-of-plane stress components play a secondary role in the diffusion-bonded sample containing the HB. This modeling assumption is further supported by the recent work of Wang et al. (Wang et al., 2024), who adopted the same rationale in their diffusion-bonded joint model. In addition, the interface properties of HB have not been independently considered because this work focus on the mechanistic link (eg. deformation compatibility between the two domains) between the micro-mechanical behaviours and the single-polycrystal structure at grain-level. Hence, the interface of HB is processed as a crystallographic boundary dividing two domains with differing material's properties.

The crystal plasticity slip rule is implemented in the user material subroutine (UMAT) using ABAQUS standard/explicit analysis. The plastic velocity gradient $\boldsymbol{L}^P$ is formulated based on crystallographic slip, incorporating both the slip directions and plane normal:

$$\boldsymbol{L}^P = \dot{\boldsymbol{F}}^p \boldsymbol{F}^{p^{-1}} = \sum_{\alpha=1}^{12} \dot{\gamma}^\alpha \boldsymbol{s}^\alpha \otimes \boldsymbol{n}^\alpha \tag{1}$$

Here, $\boldsymbol{s}^\alpha$ and $\mathbf{n}^\alpha$ represent the slip direction and the normal vector of the α^{th} slip system, respectively. $\boldsymbol{F}^P$ is the plastic deformation gradient. The corresponding slip rate $\dot{\gamma}^\alpha$ is governed by the slip rule (Dunne et al., 2007)

$$\dot{\gamma}^\alpha = \rho_{\text{ssdm}} b^2 \nu \exp\left(-\frac{\Delta F}{\mathrm{k}T}\right) \sinh\left(\frac{\Delta V}{\mathrm{k}T} \left|\tau^\alpha - \tau_{\text{c}}^\alpha\right|\right) \tag{2}$$

The model parameters are defined as follows: ρ_{ssdm} is the mobile dislocation density; b the magnitude of Burgers vector; and ν the attempt frequency. The energy barrier is characterized by the activation energy ΔF and the activation volume ΔV. The resolved shear stress on the α^{th} slip system is denoted by τ^α, while the slip system strength, τ_{c}^α, characterizes the current resistance to slip and evolves with accumulated plastic deformation through dislocation hardening by equation (3).

$$\tau_{\text{c}}^\alpha = \tau_{\text{c0}} + \alpha G b \sqrt{\rho_{\text{GND}} + \rho_{\text{SSD}}} \tag{3}$$

where the following parameters are defined: τ_{c0}, the initial intrinsic slip strength; G, the shear modulus; α, the Taylor hardening coefficient; with ρ_{SSD} and ρ_{GND} being designated as the densities of statistically stored and GNDs, respectively.

The density of sessile statistically stored dislocations, denoted as ρ_{SSD}, is empirically considered by the isotropic hardening law.

$$\dot{\rho}_{\text{SSD}} = \lambda \cdot \dot{p} \tag{4}$$

Where λ is a hardening coefficient, and p represents the effective plastic strain, which is defined by plastic strain $\boldsymbol{\varepsilon}^{\text{p}}$ as follows:

$$\dot{p} = \left(\frac{2}{3}\boldsymbol{\varepsilon}^{\text{p}} : \boldsymbol{\varepsilon}^{\text{p}}\right)^{\frac{1}{2}} \tag{5}$$

The GND density, ρ_{GND}, accommodates lattice curvature and is derived from Nye's dislocation tensor Λ (Cheng and Ghosh, 2015), which is updated at the end of each time increment:

$$\Lambda = curl\left(\boldsymbol{F}^{\boldsymbol{P}}\right) = \sum_{\alpha=1}^{12} \rho_{\text{Gs}}^\alpha \boldsymbol{b}^\alpha \otimes \boldsymbol{m}^\alpha + \rho_{\text{Get}}^\alpha \boldsymbol{b}^\alpha \otimes \boldsymbol{t}^\alpha + \rho_{\text{Gen}}^\alpha \boldsymbol{b}^\alpha \otimes \boldsymbol{n}^\alpha \tag{6}$$

Where ρ_{Gs}^α denotes the screw dislocation which aligns with slip direction $\boldsymbol{s}^\alpha$, whereas ρ_{Get}^α and ρ_{Gen}^α represent the edge dislocation components which aligns with vector $\boldsymbol{t}^\alpha$ (normal to the plane determined by $\boldsymbol{s}^\alpha$ and $\boldsymbol{n}^\alpha$) and slip normal $\boldsymbol{n}^\alpha$ respectively. The magnitude of the Burgers vector on slip system α is given by $\boldsymbol{b}^\alpha$, and $\boldsymbol{m}^\alpha$,$\boldsymbol{n}^\alpha$, and $\boldsymbol{t}^\alpha$ form an orthogonal set of unit vectors. Since the 36 independent GND components (including 12 screw and 24 edge dislocations) must be determined from only 9 available equations, equation (7) is formulated in matrix form as follows:

$$\boldsymbol{A}\boldsymbol{\rho}_{\boldsymbol{GND}} = \overline{\boldsymbol{\Lambda}} \tag{7}$$

Here, $\overline{\boldsymbol{\Lambda}}$ is the Nye dislocation tensor in 9×1 column vector form, and $\boldsymbol{A}$ denotes a 9 × 36 matrix composed of basis tensors in the form of $\boldsymbol{b}^\alpha \otimes \boldsymbol{m}^\alpha$, $\boldsymbol{b}^\alpha \otimes \boldsymbol{t}^\alpha$, and $\boldsymbol{b}^\alpha \otimes \boldsymbol{n}^\alpha$. $\boldsymbol{\rho}_{\boldsymbol{GND}}$ is a 36 × 1 column vector of GND components. Hence, a minimum L_2-norm solution is employed to minimize the weighted sum of squares of the resulting GND densities (Arsenlis and Parks, 1999). The objective function is formulated as the sum of the squares of the edge (ρ_{Get}^α, ρ_{Gen}^α) and screw (ρ_{Gs}^α) dislocation density components, resulting in a scalar measure of the GND density on each slip system (Cheng and Ghosh, 2015), expressed as:

$$\rho_{\mathrm{GND}} = \sqrt{\sum_{\alpha=1}^{12} \left(\rho_{\mathrm{Gs}}^{\alpha}\right)^2 + \left(\rho_{\mathrm{Get}}^{\alpha}\right)^2 + \left(\rho_{\mathrm{Gen}}^{\alpha}\right)^2} \tag{8}$$

Uniaxial tensile tests were carried out on the bonding sample of the single-crystal DD5 and the polycrystal FGH96. Material properties were calibrated using a sub-scale finite element model of the primary domain of interest (Fig. 2(b, c)); the calibrated material properties are shown in Table 2 and Table 3.

The three independent stiffness constants (C_{11}, C_{12} and C_{44}) were determined from experimental measurements, accounting for elastic anisotropy with a Zener ratio of 2.67 for the nickel-based superalloy (Li et al., 2021, Liang et al., 2023). Following Frost and Ashby (Frost, 1982), the activation energy ΔF was estimated as $\Delta F = \omega G b^3$, where ω is a constant reflecting the strength of dislocation obstacles. A value of $\omega = 0.04$ was adopted to represent a non strain-rate-sensitive response at room temperature, with Burgers vectors of $b = 2.54 \times 10^{-4}$ μm for the polycrystal (Chen et al., 2018) and $b = 3.51 \times 10^{-4}$ μm for the single crystal (Chen et al., 2017). The activation volume was defined as $\Delta V = \zeta b^3$, where $\zeta = 22.0$ (Zhang et al., 2021) was selected for both materials to ensure low strain-rate sensitivity under the room-temperature loading conditions considered. The initial density of mobile dislocations ρ_{ssdm} was estimated based on the previous study (Hull and Bacon, 2011).ν was the dislocation jump attempt frequency, which can be estimated as 1×10^{11} (Sweeney et al., 2013). CPFE simulations were performed to compute the tensile stress–strain responses of the monolithic FGH96, monolithic DD5 alloys and DB DD5-FGH96 sample based on the calibrated materials' properties, as shown in Fig. 3(a) and (b), in which the comparison between the experiments and CPFE shows a good agreement.

3. Results&discussion

3.1. Heterogeneous plastic strain and GND fields near the HB

To examine the microstructural evolution at varying stress levels, the same ROI in the diffusion-bonded sample was monitored under both monotonic (the 1st cycle) and the following cyclic loading (the 2nd ~5th cycle) using in-situ SEM/EBSD. Crystal orientations at each loading step (red circles in Fig. 2(d)) were used to calculate the grain reference orientation deviation (GROD), defined as the misorientation between a local orientation within a grain and the average orientation of that grain (Black et al., 2024), to quantify localized deformation near the HB. The GROD maps (Fig. 4(a–d)) reveal long-range orientation gradients within individual grains, which particularly decrease with the distance away from the HB (black narrow in Fig. 4a) in the single-crystal domain, indicating pronounced plastic deformation near the HB. CPFE simulation shows effective plastic strain evolution during in-situ tensile loading, illustrating that the single-crystal domain (right-hand side in Fig. 4) accommodates more plastic strain than the polycrystal domain (left-hand side in Fig. 4) during loading, as shown in Fig. 4(e-h).

During in-situ loading process (undeformed, the yield of the 1st cycle, peak loading of the 1st cycle, and peak loading of the 5th cycle), plastic strain localization and lattice rotation evolve progressively. In the undeformed diffusion-bonded sample (Fig. 4a), low GROD is observed near the HB, reflecting prior residual deformation introduced by bonding. At the yield of the 1st cycle (720 MPa), which beyond the yield strength of DB sample, the single-crystal domain exhibits uniform lattice rotation (dashed rectangle in Fig. 4b) and plastic strain localization near the HB (dashed ellipse in Fig. 4f). While in the polycrystal domain, the lattice rotation and plastic strain are just localized in a few grains, indicating that the single-crystal domain basically deforms first and accommodates more plastic strain, whereas the polycrystal domain, with higher slip strength and greater work-hardening capacity, constrains the single-crystal domain. Intuitively, the domain that yields first due to the lower slip strength is referred to the soft domain (single-crystal side in this work), while the domain that yields later is termed the hard domain (polycrystal side in this work) (Ding et al., 2022). As the tensile stress increasing to 810 MPa (peak loading of the 1st cycle), both single-crystal domain and polycrystal domain shows clear plastic deformation, while interfacial mechanical incompatibilities persist (Wang et al., 2019). To maintain plastic strain continuity, dislocations pile up near the HB in the single-crystal domain (the soft domain), forming GNDs that accommodate plastic incompatibility and generate interfacial plastic strain gradients (Ding et al., 2022, Lu et al., 2019). Following the first cycle peak, subsequent cyclic loading led to the continuous accumulation of GNDs near the HB within the single-crystal side (this GND density field would be discussed with more details in the following text), manifested as a progressive increase in GROD values. As cycling progresses to five cycles, this accumulation of GNDs enhances local hardening in these regions (marked by dashed ellipse in Fig. 4(f-g)). Such local hardening area is shown in Fig. 4 (i) and (j) at the peak loading of the 1st cycle and the 5th cycle, respectively. The effective plastic strain along the path A–A′ (marked in Fig. 4 (i) and (j)) show that the local hardening drives the shifting of plastic strain accumulation from the single-crystal side's HB (~7.4μm away from the HB) to the single-crystal interior (~27.5μm away from the HB) during the following cyclic loading, the concentration sites of effective plastic strain are marked by black narrows, as shown in Fig. 4(i-k).

The evolution of GND density field from the undeformed state to the 1st unloaded cycle and the 5th unloaded cycle was

Table 2
Material properties for polycrystal nickel-based superalloy FGH96.

C_{11} (GPa)	C_{12} (GPa)	C_{44} (GPa)	τ_{c0} (MPa)	b (μm)
232	148	112	370	2.54×10^{-4}
λ (μm $^{-2}$)	ν (s^{-1})	ΔF (J /atom)	ρ_{ssdm} (μm ^{2})	ΔV (μm^3)
50	1.0×10^{11}	8.2×10^{-20}	0.8	$22b^3$

Table 3
Material properties for single-crystal nickel-based superalloy DD5.

C_{11} (GPa)	C_{12} (GPa)	C_{44} (GPa)	τ_{c0} (MPa)	b (μm)
208	130	89	275	3.51×10^{-4}
λ (μm^{-2})	ν (s^{-1})	ΔF (J /atom)	ρ_{ssdm} (μm^2)	ΔV (μm^3)
200	1.0×10^{11}	9.8×10^{-20}	0.15	$22b^3$

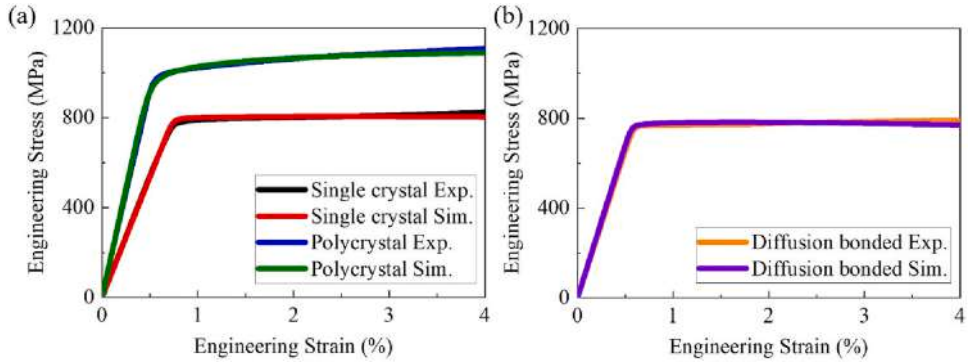

Fig. 3. Comparison of experimental and CPFE-simulated engineering stress-strain responses. (a) monolithic DD5 single-crystal and monolithic FGH96 polycrystal (b) the diffusion-bonded DD5-FGH96 heterostructure.

characterized by EBSD measurements (Fig. 5(a–c), processed by ATEX software (Beausir and Fundenberger, 2017)) and calculated by CPFE simulations (Fig. 5(d–f)), which show good agreement. The initial GND distribution (Fig. 5(a) and (d)) show a low and relatively uniform GND density field. Path B–B′ was defined near the HB within the single-crystal region of interest (Fig. 6a), which will be discussed later. The average GND density along this path, calculated from EBSD data, increased substantially from the initial value approximately 6.5×10^{12} to 3.88×10^{13} m^{-2} after the 1st cycle and further to 5.98×10^{13} m^{-2} after the 5th cycle, as shown in Fig. 6(b), which clearly shows a substantial increase in GND density near the HB in single-crystal side, indicating that the GND density is predominantly generated during cyclic deformation to accommodate plastic strain incompatibility. This evolution also reveals a rapid increase during the 1st loading cycle, followed by a significantly slower increasing rate in subsequent cycles. This trend is consistent with previous studies on the progressive GND density evolution near HB (Chen et al., 2018, Jiang et al., 2016).

The CP-computed GND density along path B-B′ shows good agreement with the in-situ EBSD measurements after the fifth cycle (Fig. 6c). Both experimental and simulation results demonstrate a heterogeneous increase in GND density with progressive cyclic loading near the HB, highlighting the pronounced plastic deformation localization near the HB. After the first cycle, pronounced dislocation pileups can be observed near the HB. With continued cyclic loading up to the fifth cycle, a markedly higher GND density is produced near the HB. The elevated GND density leads to steep plastic strain gradients and pronounced lattice curvatures. Notably, the single-crystal domain adjacent to the HB accumulates a markedly higher GND density after five cycles, while the density decreases gradually with increasing distance from the HB. This pronounced gradient demonstrates that GND accumulation is far more intense in the interfacial region than in the surrounding domains, highlighting its role as the dominant site for cyclic plastic strain localization.

The GND accumulation across the HB and the interfacial plastic strain partitioning after the 5th loading cycle were quantitatively studied using SEM and CPFE results (Fig. 7). Comparative micrographs before and after deformation (Fig. 7a, b) shows a distinct stepped morphology in the single-crystal domain. Macroscopically, this is evidenced by a progressive reduction in cross-sectional area from the interface toward the interior of the single-crystal domain (right-hand side in Fig. 7(b)). The GND density and effective plastic strain fields are shown in Fig. 7(c) and (d). The profiles along path C–C′ (marked in Fig. 7(c) and (d)) show that the single-crystal side can be subdivided into a transition zone (yellow) and a steady zone (pink) with gradually varying plastic strain and GND density, which eventually stabilize at distances farther from the HB, as shown in Fig. 7(e). It reveals a distinct contrast in mechanical field distributions across the HB is that the effective plastic strain is minimized at the HB and increases gradually into the single-crystal interior, while GND density peaks adjacent to the HB and declines with distance into the single-crystal domain, as shown in Fig. 7 (e). On the single-crystal region near the HB (yellow zone), deformation is strongly constrained by the adjacent harder polycrystal domain, leading to a reduced plastic strain compared with the interior of the single-crystal domain. In contrast, the single-crystal region far away from the HB (pink zone) experiences a rapid reduction (Fig. 7(b)), allowing the region to undergo strong plastic deformation due to the higher stress (smaller cross-sectional area), thus leading to the higher plastic strain. The sharp transition from the lower effective plastic strain within the polycrystal domain (blue zone) to the higher plastic strain within the single crystal domain (yellow zone) generates a significant plastic strain gradient, as shown in the up-side of Fig. 7(e), refers to the GND density peak near the HB (black narrow in Fig. 7(e)). Moreover, this GND density peak results in a local hardening and furtherly force the plastic strain accumulation shifting from the single-crystal side's HB to the single-crystal interior (reflected by the Fig. 4(f-h)).

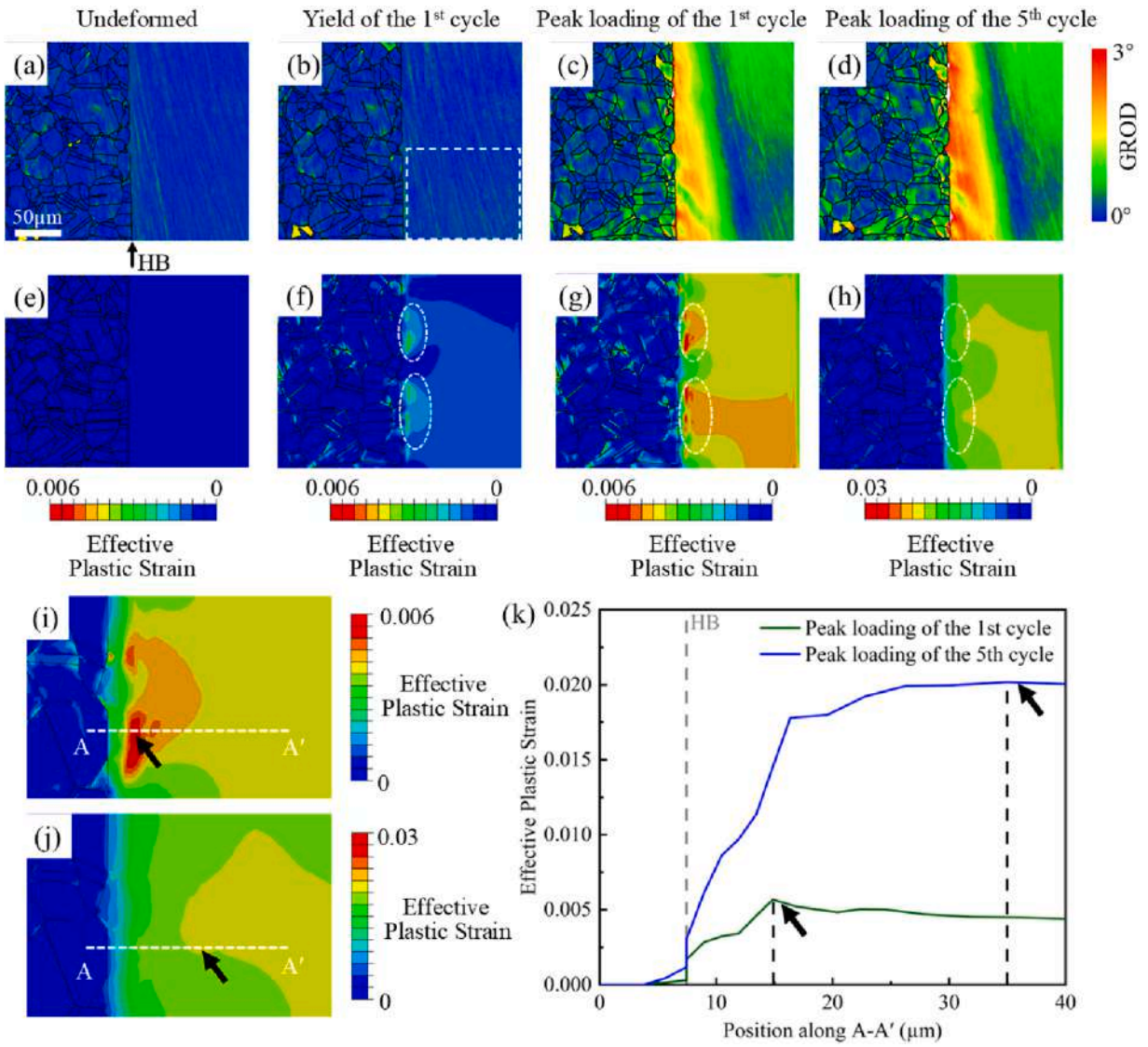

Fig. 4. Evolution of the local lattice rotation and the results of the effective plastic strain field along the HB for the polycrystal /single of the nickel-based superalloy during in-situ tensile: (a-d) EBSD images reflect local deformation details of the GROD; (e-h) Effective plastic strain field derived from CPFE simulations; (i, j) effective plastic strain at peak loading of the 1st loading cycle and the 5th loading cycles; (k) Quantitative profiles along the A–A′ path.

3.2. GND density field, elastic mismatch and crystal misorientation

In this study, the GND density field near the HB is heterogeneous (Figs. 5, 6, 7), which affects the plastic strain accumulation by dislocation hardening during the cyclic loading. Hence, investigating the mechanistic link between the microstructure and GND density field is significant in understanding the hetero-deformation in such single/polycrystal nickel-based superalloy. In this section, all of the HBs in ROI (matching 15 polycrystal grains and their common single-crystal) are extracted and marked, which refer to clear high or low GND density on the single-crystal side after the 1st cycle, as shown in Fig. 8(a-f). Dashed ellipses mark regions of low GND density in the single-crystal domain near the corresponding HB, while the other HBs indicate clear high GND density within the single-crystal side. In Fig. 8(a), high GND density regions can be observed in the single-crystal domain near the HB1 and HB2. By contrast, three low GND density regions marked by the dashed white ellipse are observed at the HB3 and HB5 within twin grain (Fig. 8b) and HB6 shown in Fig. 8(c), which demonstrates that plastic deformation compatibility can be achieved through favorable crystal orientations with low demand of GND. The rest of the HBs (HB4 shown in Fig. 8(b) and HB7-HB15 shown in Fig. 8(d-f) have a similar results as the HB1 and HB2, which are higher than the HB3, HB5 and HB6. Hence, investigating the role of crystallography on both sides of HBs is critical to the mechanistic understanding the GND density field near the HBs.

The region of low GND density near the HB within the single-crystal domain after the 1st cycle can be observed in the corresponding

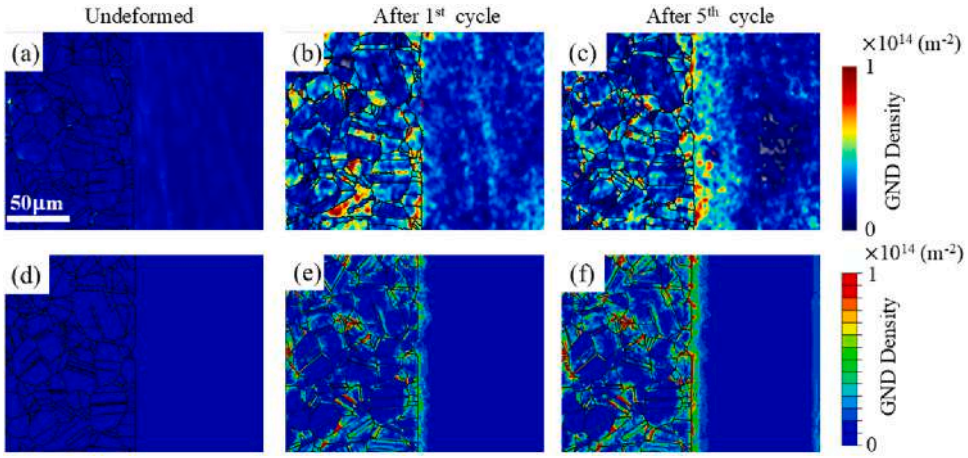

Fig. 5. Evolution of GND density distributions from experimental measurements and CPFE predictions under unloaded conditions. (a-c) Experimental results: (a) Undeformed, (b) After the 1st loading cycle, and (c) After the 5th loading cycle. (d-f) CPFE predictions: (d) initial state, (e) after the 1st loading cycle and (f) after the 5th loading cycle.

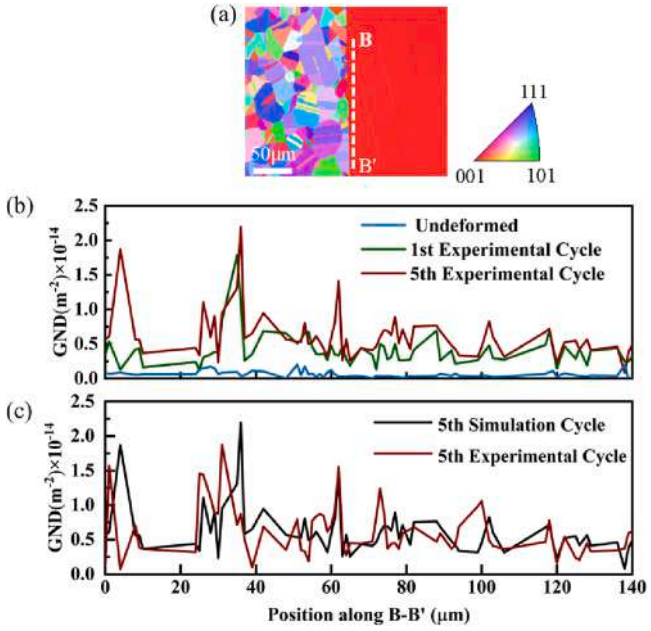

Fig. 6. (a) microstructure with corresponding paths B-B′ along which GND density is compared from CP model and EBSD;(b) the comparison of GND density along path B-B′by experiment between the end of initiation cycle and 5 cycles;(c) the comparison of GND density along path B-B′ by CPFE at the end of the 5 cycles.

IPF map of the heterostructure which is marked by white ellipse shown in Fig. 9(a). Nickel's elasticity is intrinsically anisotropy, which means the elastic mismatch near the HB would be caused by the differing crystal orientations of polycrystal grains (single domain's crystal orientation is fixed). In addition, the plastic deformation near the HB is dominated by slip, which is strongly determined by the crystal orientation. Hence, the difference of the single-crystal and polycrystal grain's crystal orientation is also significant. The following text of this section discusses the above two key factors, namely the difference of elastic modulus along the loading direction (LD) ΔE_{xx} and the <001> misorientation θ', which will be defined and calculated as follow.

The elastic modulus along the LD, denoted as E_{xx}, can be calculated based on each grain's crystallographic orientation relative to the LD. For FCC material, the Young's modulus along a specific direction E_{hkl} is given by:

$$\frac{1}{E_{hkl}} = S_{11} - 2\left(S_{11} - S_{12} - \frac{1}{2}S_{44}\right)\left(l_x^2 l_y^2 + l_y^2 l_z^2 + l_x^2 l_z^2\right) \tag{9}$$

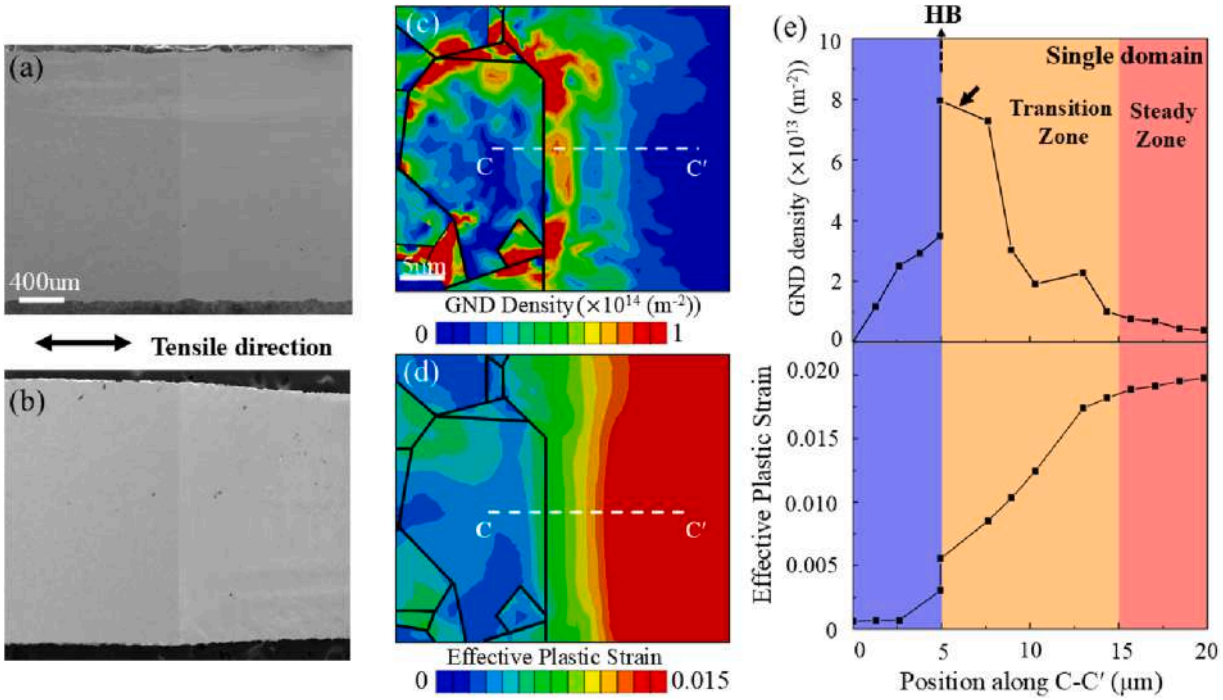

Fig. 7. Macroscopic deformation in the (a) undeformed state and (b) after five loading cycles. Local distributions of (c) GND density and (d) effective plastic strain after five loading cycles illustrate the strain gradient and GND accumulation near the HB. (e) Quantitative profiles along the C–C′ path demonstrate the partitioning of both plastic strain and GND density across the boundary.

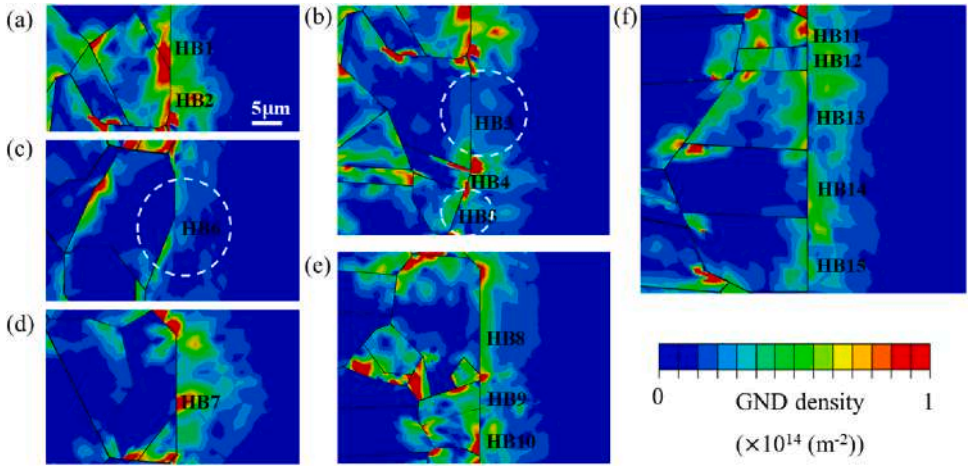

Fig. 8. Representative cases demonstrating varied GND density distributions along HB between the single crystal and polycrystalline grains after first cycle loading. (a) HB1 and HB2. (b) HB3-HB5 (c) HB6. (d) HB7 (e) HB8-HB10 (f) HB11-HB15.

where l_x, l_y and l_z are the direction cosines for crystal directions <hkl> with respect to global xyz axis. S_{11}, S_{12} and S_{44} are the three independent compliance constants which are obtained from the inverse of stiffness matrix. Fig. 9(b) is the E_{xx} map generated by the eq. (9), which clearly illustrates how the stiffness component along the loading direction results in a heterogeneous distribution of the local stiffness across the heterostructure, which governs the initial strain partitioning and the subsequent GND distribution (Latypov et al., 2021).

In this study, the <001> misorientation θ′ is defined by the minimum angle between the <001> crystal axis (including its crystallographic equivalent directions [100], [010], and [001] in the FCC system) and the LD (X-axis direction in Fig. 2(a)). In the polycrystal domain, the misorientation θ′ is calculated by the <001> most closing to the LD, while in the single-crystal domain, the <001> is chosen as the [010] because the single-crystal's [010] is almost (~3.5°) aligned with the LD. In Fig. 9(c), this misorientation θ′ is visualized for single-crystal domain (right-hand side) and each grain of polycrystal domain (left-hand side).

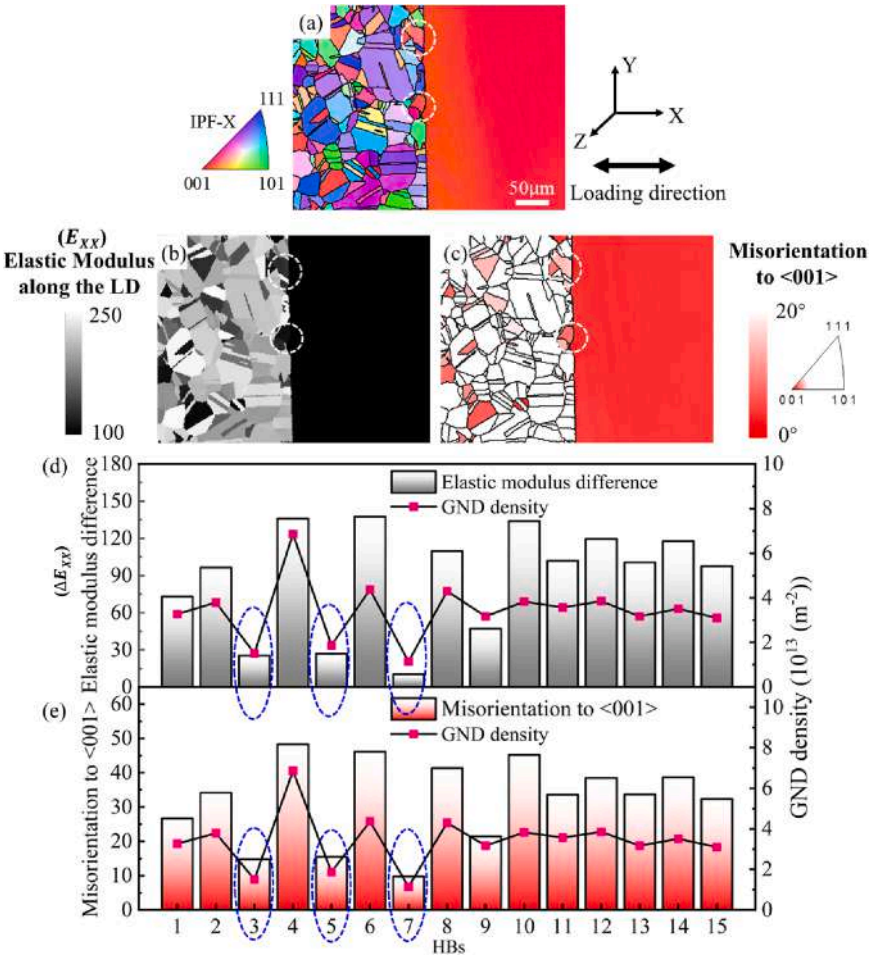

Fig. 9. Representative cases demonstrating GND density distributions after first cycle loading in an unloaded state versus the elastic modulus difference along the LD and the misorientation to <001> along HB between the single crystal and polycrystalline grains (a) Inverse pole figure (IPF-X) map of the heterostructure. (b) Distribution of elastic modulus along the LD across the heterostructure. (c) Angle between the <001> crystallographic direction of each polycrystal grain near the HB and the loading axis. (d) Correlation between elastic modulus difference and GND density along the interface. (e) Correlation between misorientation with respect to <001> and GND density along the interface.

Fig. 9 (d) shows the relationship between GND density and the difference of elastic modulus along the LD (ΔE_{xx}) for the 15 HBs studied in the last section. The GND density is affected by the elastic modulus mismatch across the HB, in which a large ΔE_{xx} between the single crystal grain and its neighboring polycrystal grain correlates with high GND density. Fig. 9(e) shows the relationship between GND density and the <001> misorientation θ', in which similar correlation can be observed as the GND density compared to the ΔE_{xx}. It shows that small <001> misorientation θ' refers to the nearly aligned lattices between the single-crystal and polycrystal domains, providing high continuity of mechanical properties. Such crystal orientation pairs (low θ') promotes coordinated deformation across the HBs under external stress, suppressing the plastic strain gradients near the HBs. As a result, the associated GND density near the HB remains low (eg. HB3, HB5 and HB7 marked by the blue ellipse). In summary, the GND density field near the HBs are jointly governed by the combined effects of elastic mismatch (ΔE_{xx}) and the crystallographic misorientation (θ') across the HB.

3.3. Slip activation and deformation compatibility near the HB

In FCC material, there are four equivalent {111} slip planes, producing four distinctive trace directions on the free surface. Based on the crystal orientations collected from EBSD scanning, the {111} slip traces of the interest of grains are shown in Fig. 10. In details, the dominant activated slip system was identified by comparing the SEM-observed slip traces with theoretical predictions and analyzing the Schmid factor (SF), in which the slip systems with the same trace and the highest SF values were considered the most likely to be activated. The dominant activated slip system is highlighted by a colored line, while the other three theoretical traces are indicated by black dashed lines. Twin boundaries are marked by blue dashed lines, and HBs are denoted by purple dashed lines.

ΔE_{xx} and <001>misorientation θ' have been demonstrated as the key microstructural features affecting the GND density field near

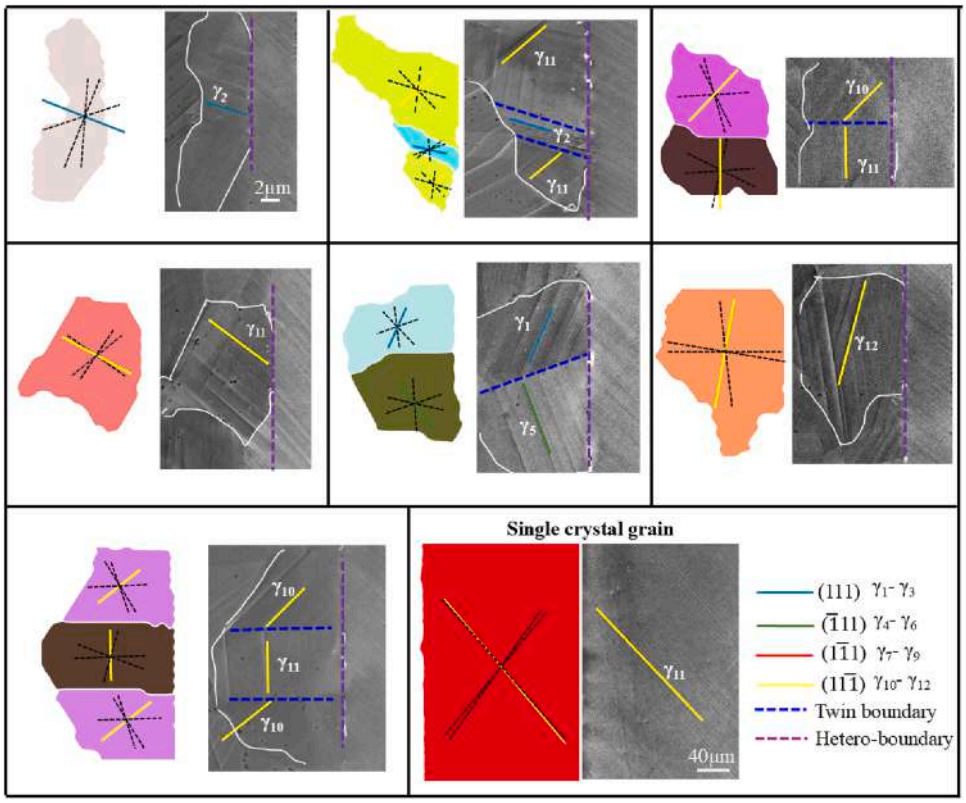

Fig. 10. The theoretical traces with SEM can confirm the {111} slip plane on the grain of interest (GOIs) with the major initiated slip system. The theoretical traces combined with the SEM can confirm the slip plane in the activated slip system.

the HB within single crystal domain. In this section, the m' parameter ($m' = \cos(\psi)\cdot\cos(\kappa)$, κ denotes the angle between slip directions of the two systems, while ψ is the angle between their slip-plane normal), proposed by Luster and Morris (Luster and Morris, 1995), quantifying slip-system coplanarity and serving as a predictive criterion for slip transmission (Escobar-Moreno et al., 2025, You et al., 2023, Liu et al., 2025), is calculated and plotted with the ΔE_{xx} and <001>misorientation θ' for all HBs in ROI to discuss their roles in GND density near the HBs within single-crystal domain after the 1st cycle, as shown in Fig. 11. The slip direction and the slip plane is determined by the highest SF on the slip plane which is validated in SEM observation as shown in Fig. 10. In Fig. 11(a), the grain pairs with low GND density (red circles, $\leq 0.25 \times 10^{14}$ m^{-2}) cluster in the lower-left corner, confirming that m' (where $m' = \cos(\psi)\cdot\cos(\kappa)$) provides a reliable criterion for GND distribution near the HB within the single-crystal. In Fig. 11(b) and (c), a threshold of $m' \geq 0.8$ also reliably identifies the low GND density, which is consistent with previous reports on slip transfer (high m′) across general grain boundaries (Chen et al., 2023).

In addition, Fig. 11(b) also shows the correlation between GND density and <001> misorientation (θ'). A clear threshold misorientation of 15° can be observed, below which GND density remains low. This suggests that when the polycrystal grain is well-aligned with the [010] axis of the single-crystal domain (nearly parallel to the LD), the interface maintains good crystallographic continuity, which corresponds to a weak plastic strain gradient and low GND density. Fig. 11(c) shows the correlation between GND density and ΔE_{xx}. A threshold value of ΔE_{xx} is observed, below which the GND density remains low, which shows a similar trend in Fig. (b), reflecting their common crystallographic determination. Fig. 11(d) further shows the relation between ΔE_{xx} and θ' to visualize the role of crystallography, demonstrating the strong dependence between the ΔE_{xx} and <001> misorientation θ' due to the FCC crystallography.

3.4. Plastic strain partitioning and deformation compatibility across the HB

Strain localization and partitioning across the HB are governed by the interaction of several factors, including crystal orientation (can be reflected by Schmid factor) (Oh et al., 2021), elastic modulus mismatch (Latypov et al., 2021), and plastic strain hardening capabilities (Wagner and Laplanche, 2023). To separate their individual influences on strain partitioning across the HB, we conducted the following three CPFE simulations.

Specifically, three cases of simulations were conducted in this part at the peak loading of the 1st cycle as shown in Fig. 12. In Case 1, both polycrystal domain (left-hand side) and the single-crystal domain (right-hand side) were assigned identical material properties of the single-crystal DD5, while their original crystal orientations were retained. Fig. 12(a) shows the polycrystal domain (left-hand-side)

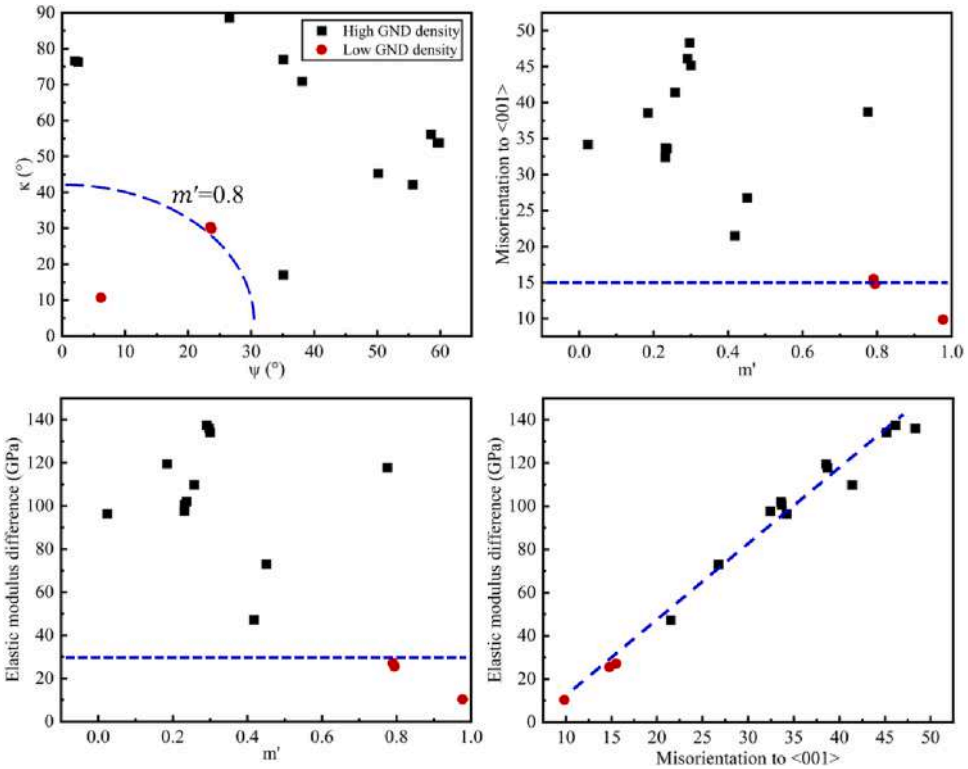

Fig. 11. Analysis of parameters influencing deformation incompatibility across the HB. (a) Angles between slip directions (κ) and slip plane normal (ψ) for calculating the geometric compatibility factor m′. (b) m′ as a function of crystallographic misorientation of the polycrystal grains near the HB relative to the <001> direction. (c) Variation of m′ with the difference in elastic modulus across the HB. (d) Relationship between elastic modulus difference and misorientation to <001>.

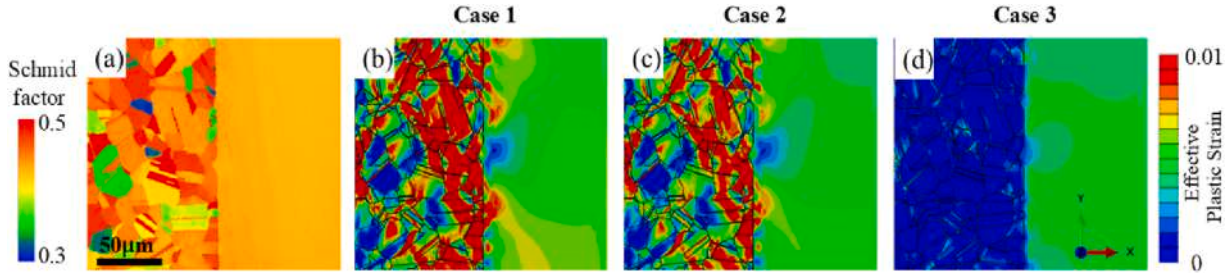

Fig. 12. Interfacial plastic strain partitioning on three cases at the peak loading of the 1st cycle: (a) Schmid factor map of the present single/polycrystal heterostructure (b) case 1: identical materials properties of single crystal DD5 (c) case 2: different elastic properties (d) case 3: different plastic hardening parameters.

with differing crystal orientation, is statistically contain a fraction of soft grains with high Schmid factors relative to the LD. In contrast, the single-crystal domain (right-hand-side) refers to a hard single grain with relative low Schmid factors relative to the LD. In Fig. 12 (b), it is clear that the effective plastic strain is higher in the polycrystal domain (left-hand-side), which illustrates that the distribution of soft grains (the grains closing to red in Fig. 12(a)) within polycrystal domain accommodates a higher magnitude of effective plastic strain due to the higher RSS on the activated slip system. However, the single-crystal domain constrained by unfavorable crystal orientation (slip activation is not strong compared with the soft grains (red grains in Fig. 12(a)) in polycrystal), exhibits lower effective plastic strain compared to the polycrystal domain, as shown in Fig. 12(b), which demonstrates that crystal orientation is an independent driver of the plastic strain partitioning across the HB.

In Case 2, the polycrystal domain (left-hand-side) and the single-crystal domain (right-hand-side) retained their own elastic modulus and crystal orientations, but both polycrystal domain and the single-crystal domain were assigned identical plastic parameters of the single-crystal DD5. The strain partitioning result (Fig. 12(c)) with only minor attenuation compared with Case 1 (Fig. 12 (a)), suggesting that the elastic modulus mismatch slightly affects the strain field driven by crystal orientation (Fig. 12(b)). Luster, J

(Latypov et al., 2021) proposed that the regions of concentrated elastic strain always serve as initiation sites for slip bands during the plastic stage, influencing the spatial distribution of subsequent plastic deformation. In Case 3, the single-crystal domain and polycrystal domain were assigned identical elastic properties of the single-crystal DD5, but retained their intrinsic plastic parameters and crystal orientations. The distribution of the effective plastic strain is reversed that the single-crystal domain (right-hand side) accommodates more plastic strain due to the lower slip strength, while the polycrystal domain shows only minor plastic strain localization in slip-favorable grains, as shown in Fig. 12(d).

The above three cases discuss the potential drivers in plastic strain partitioning (one-hand side's strain is higher), this plastic strain partitioning results in a strong plastic strain gradient near the HB, leading to local hardening by the GND accumulation. This understanding aligns with the widely accepted soft–hard domain model, explained through the principles of HDI work-hardening (Zhu and Wu, 2023, Yang et al., 2024). Fig. 13(a) schematically illustrates the GND caused by plastic strain gradient accompanying by serve lattice rotation near the HB in the single/polycrystal heterostructure. The size of the plastic strain gradient zone (marked by the yellow zone in Fig. 13(a)) which governs the magnitude of the HDI effect is influenced by the intrinsic material properties such as the stacking fault energy (SFE), strength difference between the soft and hard zones across the HB (Zhou et al., 2026). As shown in Fig. 13(b), dislocations emitted from Frank–Read sources in the soft domain and then pile up ahead of the HB, generating the local hardening near the HB (Fig. 4) that suppresses further dislocation emission in the soft region. The efficiency of GND accumulation near the HB depends on material-specific properties such as SFE. A low SFE domain is expected to produce a wider plastic strain gradient zone as it favors planar slip (Zhou et al., 2026), furtherly enhancing the local hardening near the HB (Liu et al., 2025, Wagner and Laplanche, 2023). It is noteworthy that the expansion of the plastic strain gradient zone after the 5^{th} loading cycle (Fig. 5). However, the reported observations in the heterostructures under monotonic loading indicate that the width of the plastic strain gradient zone is often observed to be remained largely constant with a magnitude of a few micrometers with increasing applied strain (Zhu and Wu, 2023, Zhou et al., 2026, Huang et al., 2018). It supports that cyclic loading can expand the size of this critical zone by the GND accumulations near the HB, which also illustrates that these accumulations refer to the resulting GND near the HB, the furtherly hardening and the shifting the plastic strain accumulation from HB to the interior of single-crystal domain (Fig. 4g).

5. Conclusion

This study investigated the hetero-deformation behavior near the HB in a single-crystal/polycrystal structure fabricated by diffusion bonding. The microstructural evolution and plastic strain partitioning mechanisms at the diffusion-bonded interface were systematically examined using a combined approach of in-situ experiments and CPFE modeling. The main conclusions are as follows:

1. The GND accumulation near the HB within the single-crystal domain accommodates plastic incompatibility, accompanied by severe lattice rotation, which induces local hardening near the HB, thereby driving the sites of plastic strain accumulation shifting from HB to the interior of the single-crystal domain during the following cyclic loading.
2. Plastic strain partitioning across the HB is associated with the crystal orientation (eg. <001> misorientation θ'), elastic mismatch ΔE_{xx} and the intrinsic slip strength on the both sides of HB, which leads to sharp plastic strain gradient (GND density) near the HB within the single-crystal domain before the shifting of plastic strain accumulation.
3. Under low incompatibility conditions (the $\theta' \leq 15^{\circ}$ or the $\Delta E_{xx} \leq 30$ GPa, in combination with a $m' \geq 0.8$), the GND density near the HB within the single-crystal domain is lower than that under high incompatibility conditions which increase the demand for GND-associated compatibility near the HB and promote a higher GND density near the HB within single-crystal domain.

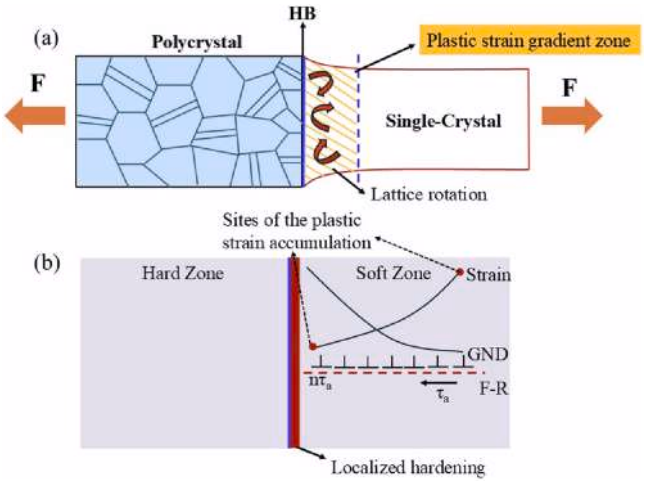

Fig. 13. (a) Application of the interfacial gradient plastic strain distribution model to the deformation mechanism of the single/polycrystal HB. (b) Schematic illustration of the strain gradient induced by GND accumulation near the HB.

CRediT authorship contribution statement

Xinrui Xiao: Writing – original draft, Methodology, Investigation, Formal analysis, Conceptualization. **Liwu Liu:** Writing – review & editing, Supervision. **Xiaoxian Zhang:** Writing – review & editing, Supervision, Methodology, Investigation, Formal analysis, Funding acquisition. **Yanju Liu:** Writing – review & editing, Supervision. **Jinsong Leng:** Writing – review & editing, Supervision.

Declaration of competing interest

The authors declare that they have no known competing financial interests or personal relationships that could have appeared to influence the work reported in this paper.

The authors acknowledge Yang Jiao, Jianxin Yu and Guanghui Hong (Center of Analysis and Measurement, Harbin Institute of Technology) for their helps in SEM, EBSD and tensile testing.

Acknowledgments

The authors acknowledge Yang Jiao, Jianxin Yu and Guanghui Hong (Center of Analysis and Measurement, Harbin Institute of Technology) for their helps in SEM, EBSD and tensile testing. This work is funded by Young Scientists Fund of the National Natural Science Foundation of China (No. 12402083) and the science foundation of national key laboratory of science and technology on advanced composites in special environments (No. JZKJW20250018-04).

Appendix A

Slip systems in FCC.

Slip system in FCC

Slip system	Slip plane normal	Slip direction
1	(111)	$[1\bar{1}0]$
2	(111)	$[01\bar{1}]$
3	(111)	$[10\bar{1}]$
4	$(\bar{1}11)$	[110]
5	$(\bar{1}11)$	$[01\bar{1}]$
6	$(\bar{1}11)$	[101]
7	$(1\bar{1}1)$	[110]
8	$(1\bar{1}1)$	[011]
9	$(1\bar{1}1)$	$[10\bar{1}]$
10	$(11\bar{1})$	$[1\bar{1}0]$
11	$(11\bar{1})$	[011]
12	$(11\bar{1})$	[101]

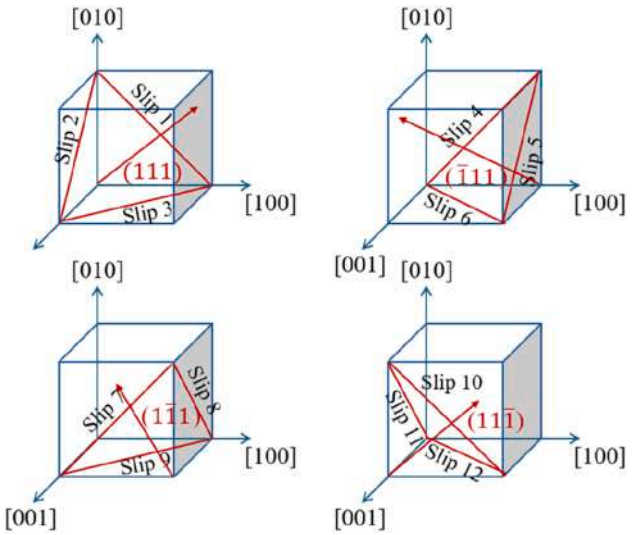

Fig. A. Identified and numbered 12 slip systems in FCC Ni that utilized in this study.

Appendix B

To valid the GND density field calculated by CPFE in this work, we plotted three parallel lines within the ROI which is line A1-A1′ 1 μm away, line B1-B1′ 5 μm away, and line C1-C1′ 10 μm away from the HB. A quantities comparison of the experimental and CPFE results along the three paths is provided in Appendix B, which demonstrates good agreement across the board.(Fig. B).

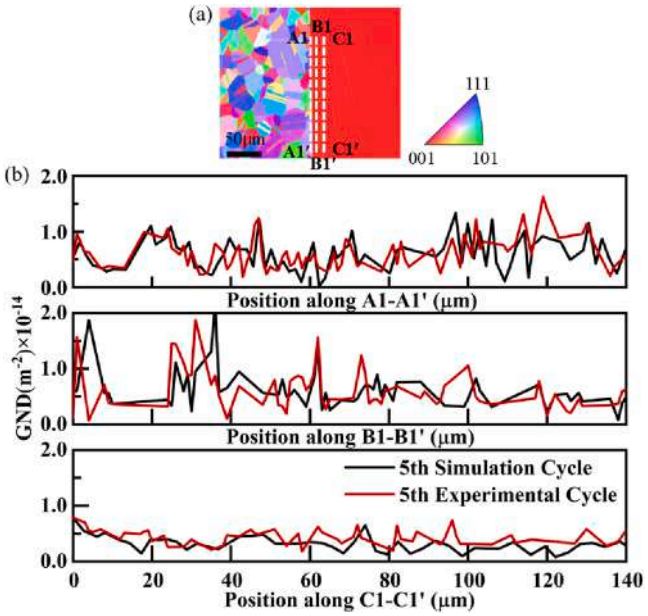

Fig. B. The distributions of GND density from EBSD measurements and CP simulations, along with line graphs comparing experimental and simulated results along three marked paths (vertical to the loading direction) after the fifth cycle (unloaded state).

Data availability

Data will be made available on request.

References

Arsenlis, A., Parks, D.M., 1999. Crystallographic aspects of geometrically-necessary and statistically-stored dislocation density. Acta Mater. 47 (5), 1597–1611. https://doi.org/10.1016/S1359-6454(99)00020-8.

Aschenbruck, J., Adamczuk, R., Seume, J.R., 2014. Recent progress in turbine blade and compressor blisk regeneration. Procedia CIRP 22, 256–262. https://doi.org/10.1016/j.procir.2014.07.016.

Beausir, B., Fundenberger, J.J., 2017. Analysis Tools For Electron and X-ray diffraction, ATEX - software. Universit´e de Lorraine - Metz. www.atex-software.eu.

Black, R.L., Anjaria, D., Genee, J., Valle, V., Stinville, J.C., 2024. Micro-strain and cyclic slip accumulation in a polycrystalline nickel-based superalloy. Acta Mater. 266, 119657. https://doi.org/10.1016/j.actamat.2024.119657.

Chen, B., Jiang, J., Dunne, F.P.E., 2017. Microstructurally-sensitive fatigue crack nucleation in Ni-based single and oligo crystals. J. Mech. Phys. Solids 106, 15–33. https://doi.org/10.1016/j.jmps.2017.05.012.

Chen, B., Jiang, J., Dunne, F.P.E., 2018. Is stored energy density the primary meso-scale mechanistic driver for fatigue crack nucleation? Int. J. Plast. 101, 213–229. https://doi.org/10.1016/j.ijplas.2017.11.005.

Chen, J., Lu, J., Cai, W., Zhang, Y., Wang, Y., Jiang, W., Rizwan, M., Zhang, Z., 2023. In-situ study of adjacent grains slip transfer of Inconel 718 during tensile process at high temperature. Int. J. Plast. 163, 103554. https://doi.org/10.1016/j.ijplas.2023.103554.

Chen, J., Li, Y., Pang, L., Wang, B., Fu, B., Yang, Y., Jia, X., 2025. The controlled incident dislocation boundaries and cell arrangements promoted multi-variant transformation and enhanced strain-hardening in a metastable ferrous medium entropy alloy. Int. J. Plast. 193, 104438. https://doi.org/10.1016/j.ijplas.2025.104438.

Cheng, J., Ghosh, S.A Crystal, 2015. Plasticity FE model for deformation with twin nucleation in magnesium alloys. Int. J. Plast. 67, 148–170. https://doi.org/10.1016/j.ijplas.2014.10.005.

Ding, H., Cui, X., Wang, Z., Zhao, T., Wang, Y., Zhang, Y., Chen, H., Huang, L., Geng, L., Chen, J., 2022. A new strategy for fabrication of unique heterostructured titanium laminates and visually tracking their synchronous evolution of strain partitions versus microstructure. J. Mater. Sci. Technol 107, 70–81. https://doi.org/10.1016/j.jmst.2021.08.016.

Dunne, F.P.E., Rugg, D., Walker, A., 2007. Lengthscale-dependent, elastically anisotropic, physically-based hcp crystal plasticity: application to cold-dwell fatigue in Ti alloys. Int. J. Plast. 23 (6), 1061–1083. https://doi.org/10.1016/j.ijplas.2006.10.013.

Escobar-Moreno, I., Nieto-Valeiras, E., LLorca, J., 2025. Slip transfer and crack initiation at grain and twin boundaries during strain-controlled fatigue of solution-hardened Ni-based alloys. Acta Mater. 283, 120497. https://doi.org/10.1016/j.actamat.2024.120497.

Frost, N., 1982. Reviews : Community Control of Social Services Departments (a Discussion Document) Peter and Suzie Beresford (1980) available from Battersea Community Action, 27 Winders Rd., Battersea, London, SW1. 40p incl. P.&p. Crit. Soc. Policy 2 (4), 113–114. https://doi.org/10.1177/026101838200200417.

Fu, X., Wu, J., Zhou, Z., Tan, M.J., Huang, Y., Sun, J., Song, W., Guan, P., Yang, Y., Li, Y., Ritchie, R.O., 2025. Interfacial strain concentration and relaxation along crystalline-amorphous boundaries of B2-reinforced bulk-metallic-glass-composites during loading. Acta Mater. 287, 120787. https://doi.org/10.1016/j.actamat.2025.120787.

González-Barrio, H., Calleja-Ochoa, A., Lamikiz, A., López de Lacalle, L.N., 2020. Manufacturing processes of integral blade rotors for turbomachinery, processes and new approaches. Appl. Sci. 10 (9), 3063. https://doi.org/10.3390/app10093063.

Griesbach, C., Bronkhorst, C.A., Thevamaran, R., 2024. Crystal plasticity simulations reveal cooperative plasticity mechanisms leading to enhanced strength and toughness in gradient nanostructured metals. Acta Mater. 270, 119835. https://doi.org/10.1016/j.actamat.2024.119835.

Hardie, C., Thomas, R., Liu, Y., Frankel, P., Dunne, F., 2022. Simulation of crystal plasticity in irradiated metals: A case study on Zircaloy-4. Acta Mater. 241, 118361. https://doi.org/10.1016/j.actamat.2022.118361.
Huang, C.X., Wang, Y.F., Ma, X.L., Yin, S., Höppel, H.W., Göken, M., Wu, X.L., Gao, H.J., Zhu, Y.T., 2018. Interface affected zone for optimal strength and ductility in heterogeneous laminate. Mater. Today 21 (7), 713–719. https://doi.org/10.1016/j.mattod.2018.03.006.
Hull, D., Bacon, D.J., 2011. Introduction to Dislocations. Elsevier.
Jiang, J., Yang, J., Zhang, T., Zou, J., Wang, Y., Dunne, F.P.E., Britton, T.B., 2016. Microstructurally sensitive crack nucleation around inclusions in powder metallurgy nickel-based superalloys. Acta Mater. 117, 333–344. https://doi.org/10.1016/j.actamat.2016.07.023.
Latypov, M.I., Stinville, J.-C., Mayeur, J.R., Hestroffer, J.M., Pollock, T.M., Beyerlein, I.J., 2021. Insight into microstructure-sensitive elastic strain concentrations from integrated computational modeling and digital image correlation. Scr. Mater. 192, 78–82. https://doi.org/10.1016/j.scriptamat.2020.10.001.
Li, P., Jiang, W., Rui, S.-S., Yao, W., Shi, H., Han, Q., Huang, J., 2021. Effect of misorientation on the fatigue life of nickel-base single crystal superalloy DD5 at 980°C. Int. J. Fatigue 153, 106479. https://doi.org/10.1016/j.ijfatigue.2021.106479.
Li, S., Li, J., Shi, J., Peng, Y., Peng, X., Sun, X., Jin, F., Xiong, J., Zhang, F., 2022. Microstructure and mechanical properties of transient liquid phase bonding DD5 single-crystal superalloy to CrCoNi-based medium-entropy alloy. J. Mater. Sci. Technol 96, 140–150. https://doi.org/10.1016/j.jmst.2021.04.024.
Li, Z., Zhang, L., Svendsen, B., Xue, Q., Tang, S., Ma, Y., Liu, W., 2024. Heterogeneous phase deformation in a dual-phase tungsten alloy mediated by the tungsten/matrix interface: insights from compression experiments and crystal plasticity modeling. Int. J. Plast. 183, 104156. https://doi.org/10.1016/j.ijplas.2024.104156.
Li, J., Ma, X., Lu, K., Wang, Y., Zhu, Y., 2025. Unusual deformation mechanisms evoked by hetero-zone interaction in a heterostructured FCC high-entropy alloy. Acta Mater. 282, 120516. https://doi.org/10.1016/j.actamat.2024.120516.
Liang, Z., Wang, X., Cui, Y., Xu, W., Zhang, Y., He, Y., 2023. A new data-driven probabilistic fatigue life prediction framework informed by experiments and multiscale simulation. Int. J. Fatigue 174, 107731. https://doi.org/10.1016/j.ijfatigue.2023.107731.
Liu, S., Nambu, S., 2024. Effect of plastic deformability and fracture behaviour on interfacial toughening mechanism at Fe/Ni interfaces. Int. J. Plast. 181, 104107. https://doi.org/10.1016/j.ijplas.2024.104107.
Liu, Y., Cao, Y., Mao, Q., Zhou, H., Zhao, Y., Jiang, W., Liu, Y., Wang, J.T., You, Z., Zhu, Y., 2020. Critical microstructures and defects in heterostructured materials and their effects on mechanical properties. Acta Mater. 189, 129–144. https://doi.org/10.1016/j.actamat.2020.03.001.
Liu, T., Zhang, X., Song, W., Li, C., Wang, P., Li, D., Zhu, Y., Li, Y., 2025. Dynamic hetero-deformation induced hardening through strength reversal between hetero-zones in austenite-ferrite duplex steel. Acta Mater. 293, 121120. https://doi.org/10.1016/j.actamat.2025.121120.
Liu, S., Cheng, J., Zhang, C., Zhu, W., Song, K., Tian, R., 2025. Effect of hydrides on deformation mechanism and slip transfer behavior of Zr-4 alloy during tensile deformation. Mater. Charact. 230, 115672. https://doi.org/10.1016/j.matchar.2025.115672.
Lu, X., Zhang, X., Shi, M., Roters, F., Kang, G., Raabe, D., 2019. Dislocation mechanism based size-dependent crystal plasticity modeling and simulation of gradient nano-grained copper. Int. J. Plast. 113, 52–73. https://doi.org/10.1016/j.ijplas.2018.09.007.
Luster, J., Morris, M.A., 1995. Compatibility of deformation in two-phase Ti-Al alloys: dependence on microstructure and orientation relationships. Met. Mater Trans. A 26 (7), 1745–1756. https://doi.org/10.1007/BF02670762.
Ma, H., Zhao, Y., Lyu, Z., Wang, X., Zhu, Y., Gao, Y., 2023. What are the "dispersive shear bands" on the surfaces of layered heterostructured materials? J. Mech. Phys. Solids 181, 105467. https://doi.org/10.1016/j.jmps.2023.105467.
Najmabad, S.I., Fullwood, D., Russell, T., Knezevic, M., Miles, M., 2024. Interpretation of the stress dip test as a means of characterizing backstress: experiments and backstress-aided crystal plasticity modeling of polycrystalline tantalum. Int. J. Plast. 181, 104089. https://doi.org/10.1016/j.ijplas.2024.104089.
Nie, Z., Wang, F., Li, J., Liu, C., Zhao, C., Sanandiya, S., Calvat, M., Anjaria, D., Zeng, J., Dong, S., Wang, F., Jin, L., Dong, J., Stinville, J.-C., 2025. Strain localization induced by closely spaced lamellae structure in a Mg alloy containing long period stacking ordered structure. Int. J. Plast. 193, 104423. https://doi.org/10.1016/j.ijplas.2025.104423.
Oh, H.S., Biggs, K., Güvenç, O., Ghassemi-Armaki, H., Pottore, N., Tasan, C.C., 2021. *In-situ* investigation of strain partitioning and microstructural strain path development up to and beyond necking. Acta Mater. 215, 117023. https://doi.org/10.1016/j.actamat.2021.117023.
Peng, Y., Li, J., Li, S., Chen, Y., Li, Z., Guo, W., Xiong, J., 2022. Microstructure evaluation and fracture mechanism of dissimilar diffusion bonded joint of single crystal superalloy DD5 and polycrystalline superalloy GH4169. Mater. Charact. 189, 111999. https://doi.org/10.1016/j.matchar.2022.111999.
Peterson, G.R., Jeong, Y., Tomé, C.N., Sangid, M.D., 2024. A comprehensive analysis of cermet design and thermal cyclic stability via elasto-viscoplastic crystal plasticity modeling. Int. J. Plast. 179, 104032. https://doi.org/10.1016/j.ijplas.2024.104032.
Qu, P., Yang, W., Wang, Q., Liu, C., Qin, J., Zhang, J., Liu, L., 2024. Unveiling the orientation sensitivity of creep life in near [001]oriented Ni-based single crystal superalloys at intermediate temperatures. Int. J. Plast. 179, 104035. https://doi.org/10.1016/j.ijplas.2024.104035.
Ran, H., Ye, P., Guo, F., Wang, M., Su, W., Chen, X., Gao, S., Tsuji, N., Zhu, Y., Lu, X., Huang, C., 2024. Superior strength-ductility combination resulted from hetero-zone boundary affected region in Cu-Fe layered material. J. Mater. Sci. Technol. 181, 209–219. https://doi.org/10.1016/j.jmst.2023.09.027.
Raza, M.H., Wasim, A., Hussain, S., Sajid, M., Jahanzaib, M., 2019. Grain selection and crystal orientation in single-crystal casting: State of the art. Cryst. Res. Technol. 54 (2), 1800177. https://doi.org/10.1002/crat.201800177.
Ren, N., Li, J., Panwisawas, C., Xia, M., Dong, H., Li, J., 2022. Insight into the sensitivities of freckles in the directional solidification of single-crystal turbine blades. J. Manuf. Process. 77, 219–228. https://doi.org/10.1016/j.jmapro.2022.03.019.
Šajbanová, K., Čerňan, J., Škultéty, F., Rostáš, J., 2021. Conceptual design of the axial compressor stage with counter-rotating rotors. Transp. Res. Procedia 59, 144–153. https://doi.org/10.1016/j.trpro.2021.11.106.
Sato, A., Chiu, Y.-L., Reed, R.C., 2011. Oxidation of nickel-based single-crystal superalloys for industrial gas turbine applications. Acta Mater. 59 (1), 225–240. https://doi.org/10.1016/j.actamat.2010.09.027.
Shi, J., Liu, J., Jin, F., Tian, F., Sun, X., 2023. Diffusion bonding of FGH98 superalloy and DD5 single crystal using pure Ni interlayer. Mater. Today Commun. 37, 107003. https://doi.org/10.1016/j.mtcomm.2023.107003.
Sun, Y.T., Kong, X., Wang, Z.B., 2022. Superior mechanical properties and deformation mechanisms of a 304 stainless steel plate with gradient nanostructure. Int. J. Plast 155, 103336. https://doi.org/10.1016/j.ijplas.2022.103336.
Sweeney, C.A., Vorster, W., Leen, S.B., Sakurada, E., McHugh, P.E., Dunne, F.P.E., 2013. The role of elastic anisotropy, length scale and crystallographic slip in fatigue crack nucleation. J. Mech. Phys. Solids 61 (5), 1224–1240. https://doi.org/10.1016/j.jmps.2013.01.001.
Wagner, C., Laplanche, G., 2023. Effects of stacking fault energy and temperature on grain boundary strengthening, intrinsic lattice strength and deformation mechanisms in CrMnFeCoNi high-entropy alloys with different Cr/Ni ratios. Acta Mater. 244, 118541. https://doi.org/10.1016/j.actamat.2022.118541.
Wang, Y.F., Wang, M.S., Fang, X.T., Guo, F.J., Liu, H.Q., Scattergood, R.O., Huang, C.X., Zhu, Y.T., 2019. Extra strengthening in a coarse/ultrafine grained laminate: role of gradient interfaces. Int. J. Plast. 123, 196–207. https://doi.org/10.1016/j.ijplas.2019.07.019.
Wang, Y., Huang, C., Li, Y., Guo, F., He, Q., Wang, M., Wu, X., Scattergood, R.O., Zhu, Y., 2020. Dense dispersed shear bands in gradient-structured Ni. Int. J. Plast. 124, 186–198. https://doi.org/10.1016/j.ijplas.2019.08.012.
Wang, J., Liang, J., Zhang, D., Peng, Y., Wen, Z., 2023. The effect of small orientation deviation from [001]to [011]on high-temperature creep properties of nickel-based single crystal. Int. J. Plast. 166, 103648. https://doi.org/10.1016/j.ijplas.2023.103648.
Wang, W., Balint, D.S., Shirzadi, A.A., Wang, Y., Lee, J., Aucott, L., Jiang, J., 2023. Imparted benefits on mechanical properties by achieving grain boundary migration across voids. Acta Mater. 256, 119103. https://doi.org/10.1016/j.actamat.2023.119103.
Wang, J., Wang, H., Gao, H., Cheng, F., Zhang, B., Zhang, M., Cheng, X., Zhang, S., Liu, D., 2024. Microstructure characteristics and failure mechanisms of hybrid manufacturing of FGH96 and IC10 bimetal component using laser directed energy deposition. Mater. Sci. Eng. A-Struct. Mater. Prop. Microstruct. Process 889, 145965. https://doi.org/10.1016/j.msea.2023.145965.
Wang, W., Zhang, R., Shirzadi, A.A., Balint, D.S., Aucott, L., Jiang, J., 2024. Thermal cracking: clarifying the effects of phases, voids and grains through characterisation and crystal plasticity modelling. J. Mech. Phys. Solids 186, 105600. https://doi.org/10.1016/j.jmps.2024.105600.

Wu, T., Zhang, Q., Lu, H., Shi, Y., Zhang, Q., Zhang, S., Wang, R., Lin, P., Lin, T., He, P., 2023. Diffusion brazing of GH536 polycrystalline superalloy with IC10 single crystal superalloy using BNi-2 interlayer. J. Mater. Res. Technol. 24, 9850–9865. https://doi.org/10.1016/j.jmrt.2023.05.223.

Xu, X., Kumar, P., Cao, R., Ye, Q., Chu, Y., Tian, Y., Li, Y., Ritchie, R.O., 2024. Exceptional cryogenic-to-ambient impact toughness of a low carbon micro-alloyed steel with a multi-heterogeneous structure. Acta Mater. 274, 120019. https://doi.org/10.1016/j.actamat.2024.120019.

Yang, Z., Liu, X., Zhao, J., Zeng, Q., Xu, K., Li, Y., Wang, C., Wang, L., Li, J., Wang, J., Kim, H.S., Wang, Z., He, F., 2024. Discontinuous coarsening leads to unchanged tensile properties in high-entropy alloys with different recrystallization volume fractions. Int. J. Plast. 176, 103963. https://doi.org/10.1016/j.ijplas.2024.103963.

You, X., Yang, J., Dan, C., Shi, Q., Zhong, S., Wang, H., Chen, Z., 2023. Statistical analysis of slip transfer in Al alloy based on *in-situ* tensile test and high-throughput computing method. Int. J. Plast. 166, 103649. https://doi.org/10.1016/j.ijplas.2023.103649.

Zan, X.D., Guo, X., Weng, G.J., 2025. Simulation of fracture behaviors in hydrogenated zirconium alloys using a crystal plasticity coupled phase-field fracture model. Int. J. Plast. 188, 104304. https://doi.org/10.1016/j.ijplas.2025.104304.

Zhang, X., Stinville, J.-C., Pollock, T.M., Dunne, F.P.E., 2021. Crystallography and elastic anisotropy in fatigue crack nucleation at nickel alloy twin boundaries. J. Mech. Phys. Solids 155, 104538. https://doi.org/10.1016/j.jmps.2021.104538.

Zhang, X., Zhao, J., Kang, G., Zaiser, M., 2023. Geometrically necessary dislocations and related kinematic hardening in gradient grained materials: A nonlocal crystal plasticity study. Int. J. Plast. 163, 103553. https://doi.org/10.1016/j.ijplas.2023.103553.

Zhang, Y., He, C.-Y., Wang, X., Hama, T., Sun, B., Jia, Y.-F., Zhang, X.-C., Tu, S.-T., 2024. Revealing the fatigue strengthening and damage mechanisms of surface-nanolaminated gradient structure. Int. J. Plast. 182, 104128. https://doi.org/10.1016/j.ijplas.2024.104128.

Zhang, Z., Shen, F., Ke, L.-L., 2024. A dislocation density-based crystal plasticity damage model for rolling contact fatigue of gradient grained structures. Int. J. Fatigue 179, 108038. https://doi.org/10.1016/j.ijfatigue.2023.108038.

Zhao, J., Zhang, X., Lu, S., Liu, D., Chen, H., Kang, G., 2025. A physically grounded model for size effects in the initial yielding of metallic materials with deformation heterogeneity. Int. J. Plast. 189, 104345. https://doi.org/10.1016/j.ijplas.2025.104345.

Zhou, H., Huang, C., Sha, X., Xiao, L., Ma, X., Höppel, H.W., Göken, M., Wu, X., Ameyama, K., Han, X., Zhu, Y., 2019. In-situ observation of dislocation dynamics near heterostructured interfaces. Mater. Res. Lett. 7 (9), 376–382. https://doi.org/10.1080/21663831.2019.1616330.

Zhou, C., Hu, W., Le, Q., Lin, Y., Wang, T., Jeon, H., Liao, Q., Hu, C., Liu, L., Zhu, Y., Xie, X., 2025. Revealing the underlying slip/twinning mechanisms of tension-compression asymmetry and anisotropy in Mg-Gd-Y-Zn-Zr alloys with heterostructure. Int. J. Plast. 194, 104493. https://doi.org/10.1016/j.ijplas.2025.104493.

Zhou, H., Wu, X., Srolovitz, D., Zhu, Y., 2026. Designing heterostructured materials. Nat. Mater. 1–7. https://doi.org/10.1038/s41563-025-02444-y.

Zhu, Y., Wu, X., 2023. Heterostructured materials. Prog. Mater. Sci. 131, 101019. https://doi.org/10.1016/j.pmatsci.2022.101019.

Zou, T., Lang, Z., Chen, H., Ye, Z., Wu, T., Wang, W., Yang, J., Huang, J., 2024. Rapidly achieving high-performance joining of single crystal superalloy and powder metallurgy superalloy via partial transient liquid phase diffusion bonding. J. Manuf. Process 109, 79–88. https://doi.org/10.1016/j.jmapro.2023.12.009.